

Torsion experiments on coarse-grained dunite: implications for microstructural evolution when diffusion creep is suppressed

PHILIP SKEMER^{1*}, MARSHALL SUNDBERG², GREG HIRTH³ & REID COOPER³

¹Washington University in Saint Louis, Saint Louis, MO 63130

²University of Minnesota, Minneapolis, MN 55455, USA

³Department of Geological Sciences, Brown University, Providence, RI 02920, USA

*Corresponding author (e-mail: pskemer@wustl.edu)

Abstract: Large strain deformation experiments in torsion were conducted on a coarse-grained natural dunite with a pre-existing lattice preferred orientation (LPO). Experiments were conducted at conditions where deformation by diffusion creep is initially negligible. Microstructural evolution was studied as a function of strain. We observe that the pre-existing LPO persists to a shear strain of at least 0.5. At larger strains, this LPO is transformed. Relict deformed grains exhibit LPO with [100] crystallographic axes at high angles to the shear plane. Unlike previous experimental studies, these axes do not readily rotate into the shear plane with increasing strain. Partial dynamic recrystallization occurs in samples deformed to moderate strains ($\gamma > 0.5$). Recrystallized material forms bands that mostly transect grain interiors. The negligible rate of diffusion creep along relict grain boundaries, as well as the limited nature of dynamic recrystallization, may account for the relatively large strains required to observe evolution of microstructures. Our data support hypotheses based on natural samples that microstructures may preserve evidence of complex deformation histories. Relationships between LPO, seismic anisotropy and deformation kinematics may not always be straightforward.

As the most abundant mineral in the upper mantle, olivine plays a key role its rheological behaviour (Karato & Wu 1993; Hirth & Kohlstedt 2003). Moreover, olivine is essential to our interpretation of mantle kinematics because of its strong influence on seismic anisotropy (Nicolas & Christensen 1987; Karato *et al.* 2008). The generation and evolution of olivine lattice preferred orientation (LPO) has been well documented in laboratory studies (Carter & Ave Lallemand 1970; Nicolas *et al.* 1973; Zhang & Karato 1995; Bystricky *et al.* 2000; Zhang *et al.* 2000; Jung & Karato 2001), naturally deformed peridotites (Nicolas *et al.* 1971; Mercier 1985; Ben Ismail & Mainprice 1998; Warren *et al.* 2008; Skemer *et al.* 2010) and numerical simulations (Wenk *et al.* 1991; Wenk & Tomé 1999; Tommasi *et al.* 2000; Kaminski & Ribe 2001; Blackman & Kendall 2002; Castelnaud *et al.* 2009). However, there are still substantial differences between the microstructures generated or observed in these studies. Notably, studies of peridotite mylonites suggest that somewhat larger strains may be required to rotate LPO into concordance with deformation kinematics, in comparison to experimental studies and numerical simulations that have an initially random texture (Warren *et al.* 2008). This difference in the influence of strain on LPO may be a consequence of factors such as the initial

microstructure and the conditions of deformation. Furthermore, different numerical models show distinct patterns and rates of LPO development which may differ from experimental and geological observations (Castelnaud *et al.* 2009). Variations between models arise from differences in numerical techniques, but also the inclusion or exclusion of specific dynamic recrystallization mechanisms (Wenk *et al.* 1991; Wenk & Tomé 1999). To expand on existing experimental studies and provide further bases for numerical investigations, we conducted a series of deformation experiments on coarse-grained natural dunite. The objective of these experiments is to improve our understanding of microstructural processes in realistic mantle materials and to help bridge the gap between the laboratory and nature.

For technical reasons, many of the experimental studies of olivine deformation have been conducted on relatively fine-grained synthetic materials (e.g. Zhang & Karato 1995; Bystricky *et al.* 2000). As a consequence, deformation in these experiments typically includes contributions from several parallel mechanisms including dislocation creep, diffusion creep and grain-boundary sliding (Fig. 1). In contrast, many geologically observable mantle rocks are interpreted to have deformed at conditions where dislocation creep is strongly dominant. It is therefore important to understand from an

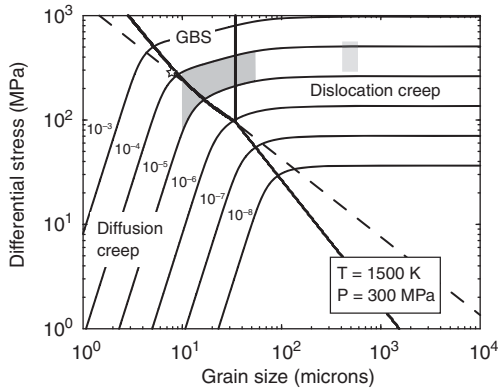


Fig. 1. Deformation mechanism map of olivine at $T = 1500$ K, $P = 300$ MPa and at dry conditions, using flow laws from Hirth & Kohlstedt (2003). Thick lines demark boundaries between deformation mechanisms: dislocation creep, diffusion creep and grain-boundary sliding (GBS). The dashed line is the location of the olivine recrystallized grain-size piezometer. Thin lines are contours of constant strain rate. The dark shaded region shows the conditions of experiments for typical hot-pressed aggregates. The light shaded region shows the conditions of the experiments in this study. Curvature in the strain-rate contours shows regions in deformation space where multiple mechanisms play a significant role in deformation. The white star on the piezometer line shows the recrystallized grain size for sample PIP-21.

experimental perspective how mantle materials deform when grain-size-sensitive creep is more completely suppressed.

To this end, we conducted laboratory deformation experiments on samples cored from a block of Balsam Gap Dunite, which was chosen for two reasons. First, it has a moderately large grain size which allows us to suppress activity of the diffusion creep mechanism. Secondly, it has a moderately strong pre-existing LPO. This allows us to consider how LPO might evolve in a situation where kinematics are changing, for example in a corner flow regime such as a mantle wedge or mid-ocean ridge.

Methods

Coarse-grained olivine aggregates were deformed in torsion in the Paterson gas medium apparatus at Brown University and at the University of Minnesota. Paterson apparatus were used because of their relatively large sample volume ($c. 1 \text{ cm}^3$) and their ability to deform materials to large strains. Starting materials were cored from a clean block of Balsam Gap Dunite, which is largely devoid of visible

alteration (Fig. 2). The initial grain size of the starting material is $510 \pm 100 \mu\text{m}$, as determined by the mean intercept technique with a stereological correction factor of 1.7. The grains are equant, with straight or gently curved grain boundaries and 120° triple junctions. A few grains have subgrain boundaries, but most do not exhibit any undulose extinction that would indicate the presence of many dislocations. The material contains $c. 1\%$ spinel and no other secondary phases are visible. The water content in the starting material is below the detection limit of Fourier Transform Infrared Spectroscopy (FTIR) (< 30 ppm H/Si).

Two experimental challenges must be overcome to deform coarse-grained dunite in torsion. First, due to the strength of these materials, a relatively large torque must be applied to the sample to achieve flow at reasonable experimental strain rates. Second, to apply a large torque to the sample there must be sufficient frictional traction between the sample and the forcing pistons to mitigate sliding along these interfaces. To solve these two problems we used a 'dog-bone' shaped sample which is wide at the ends and tapered to a narrow cylindrical central region (Fig. 3). The wide ends of the samples provide sufficient contact area with the pistons to support moderately large torques. These torques are then concentrated into the central cylindrical region of the sample, exploiting the strong radial dependence between shear stress (τ) and torque (M) in a cylindrical

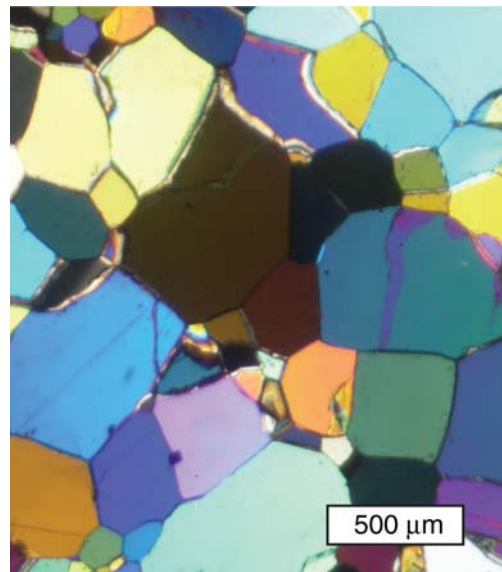


Fig. 2. Photomicrograph of the Balsam Gap Dunite, the starting material for these experiments.

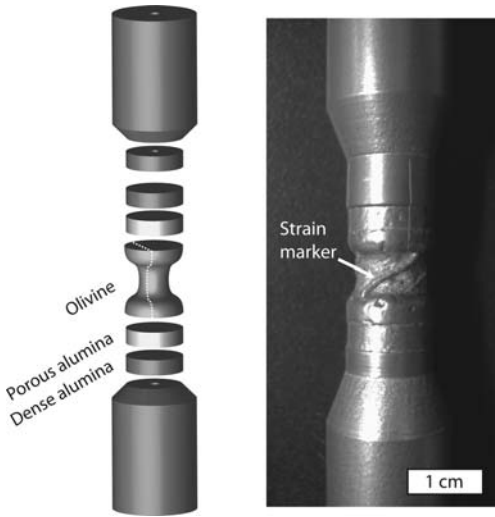


Fig. 3. Sample assembly. Dog-bone-shaped olivine samples are sandwiched between a series of alumina pistons and spacers. The white dashed line marks the location of the tangent sections from which the microstructure is analysed. Kinks that form when the iron jacket is swaged around the sample are used to measure shear strain. The example shown here corresponds to a maximum shear strain of $\gamma = 1.8$.

geometry (Paterson & Olgaard 2000) where d is the sample diameter and n is the stress exponent for a power-law material (Equation 1):

$$M = \frac{\pi d^3 \tau}{4(3 + 1/n)}. \quad (1)$$

Relatively large stresses can therefore be achieved with relatively small torques. This is similar to the solution adopted by Bystricky *et al.* (2000), who allowed sintered hot-presses to collapse down into a tapered shape during densification prior

to deformation (M. Bystricky, pers. comm. 2008). By introducing the tapered shape in a controlled fashion, we are able to achieve more consistent and reproducible results.

To make the dog-bone shape, cores were placed in a lathe and a central section was ground down using a high-speed rotary tool and diamond burr. The narrow region had a constant diameter of 6.4–7.0 mm over a length of *c.* 3.0 mm, which transitioned to the full diameter of 9.8 mm over a length of *c.* 2.0 mm. The transition between the centre and the ends of the sample has continuous curvature with a radius of *c.* 1 mm. This curvature was introduced to prevent puncturing the jacket material during compression. The ends of the sample were faced and sandwiched between porous alumina pistons, which help grip the sample (Fig. 3). Sample assemblies were dried overnight in a vacuum oven at 400 K prior to deformation. The narrow span of the sample was wrapped with Ni foil and the whole assembly was jacketed in iron, which was collapsed around the sample by briefly increasing the confining pressure to 110 MPa. This cinching of the jacket introduced creases, which are used for calculating shear strain (Fig. 3). Score marks, drawn with a razor blade normal to the shear plane, are also used to calculate shear strain and to confirm that slipping on sample–piston interfaces did not occur.

Experiments were conducted at constant twist rates of 25–50 micro-rad/s at fixed temperature and pressure (1500 K; 300–315 MPa), to a range of shear strains. Because of slight differences in the effective sample length, these twist rates produced a range of strain rates as recorded in Table 1. All experiments were run until ruptures in the iron jacket occurred, reducing the effective confining pressure to zero and effectively terminating the experiment.

The mechanical data directly recorded by the Paterson apparatus are the twist rate (with units of radians/second) and the torque applied to the

Table 1. Sample table

Sample*	Pressure (MPa)	Temperature (K)	Maximum shear strain	Maximum shear strain rate (1/s)
PIP-19	310	1500	0.2	2.2×10^{-5}
PIP-20	315	1500	1.2	4.8×10^{-5}
PIP-21	315	1500	1.8	3.5×10^{-5}
PIP-22†	315	1500	3.9	2.8×10^{-5} to 3.1×10^{-4}
PT-0474	300	1500	0.5	1.9×10^{-4}
PT-0484	300	1500	3.5	1.9×10^{-4}

*Experiments numbered PIP and PT conducted at Brown University and University of Minnesota, respectively.

†Some strain-rate stepping was done at the beginning of this run.

sample. The maximum strain rate is calculated from the imposed twist rate and the dimensions of the narrow span of the dog bone:

$$\dot{\gamma}_{\max} = \frac{d\dot{\theta}}{2l} \quad (2)$$

where $\dot{\gamma}_{\max}$ is the maximum shear strain rate, d is the sample diameter, l is the length of the sample and $\dot{\theta}$ is the imposed twist rate (Paterson & Olgaard 2000). The maximum strain rate is also determined from the deflection of the passive strain marker and the duration of the experiment. Strain calculated from the deflection of the strain marker tends to be slightly higher than strain calculated from equation (2), as some twist is inhomogeneously accommodated by the sample where it transitions from narrow to wide. We therefore report only the strains calculated from the deflection of the strain marker. Shear stress is calculated from the torque record using equation (1) assuming all deformation is partitioned into the narrow span of the sample. Shear strain and shear strain rate are a linear function of radius, with the maximum values occurring at the outer edge of the sample. Like strain, the stress state within the specimen varies both radially and axially due to the cylindrical geometry and tapered dog-bone shape. Because of the non-linear rheology predicted from flow laws and inferred from these measurements, most of the torque is supported by the outermost annulus of the cylindrical sample (Paterson & Olgaard 2000). Within this outermost annulus, torque is proportional to stress. Assuming that the total measured torque is proportional to the shear stress in the outermost shell of the specimen, the relationship between torque and maximum shear strain rate is analogous to a standard constitutive equation:

$$\dot{\gamma}_{\max} \propto M^n \quad (3)$$

where M is torque and n is equivalent to the stress exponent.

After recovering the samples, thin sections were made through a tangent section as close as possible to the edge of the deformed portion of the sample (Fig. 3). Tangent sections were used for analysis because the kinematics of deformation are nearly identical across the section. LPO was measured using electron backscatter diffraction (EBSD) on a JEOL 845 or JEOL 7001FLV scanning electron microscope with 20 mm working distances and 20 kV accelerating voltage. EBSD measurements were made on both the undeformed and deformed portions of the samples, to determine both the initial and final LPO. Undeformed regions were mapped automatically with 50 micron steps, while deformed regions were mapped with 10 micron

steps. Datasets were processed to eliminate erroneous data spikes, and reduced to one point per grain. Only grains with at least 5 contiguous pixels of the same orientation are used when plotting the pole figures of the relict grains. In experiments conducted to larger strains, EBSD was used to investigate the microstructures produced by dynamic recrystallization. These recrystallized regions were mapped with 0.25 micron steps, and the datasets were also processed to remove wild spikes. A minimal amount of smoothing was applied to fill gaps in the data.

Results

Rheological data

Figure 4 shows mechanical data from these experiments. In Figure 4a, stress–strain curves are shown for experiments conducted at strain rates of $2.2\text{--}4.8 \times 10^{-5} \text{ s}^{-1}$ (in black) and $1.9 \times 10^{-4} \text{ s}^{-1}$ (in grey). The higher strain-rate experiments achieve peak stresses at shear strains of *c.* 0.25, followed by significant decreases in strength. The lower strain-rate experiments do not show significant strain weakening. Shear stresses calculated from the torque record using equation (1) are much higher than predicted from flow laws (Fig. 1). As we discuss later, this is likely an artefact of the sample shape and deformation geometry.

To constrain the deformation regime in these experiments, strain-rate stepping experiments were conducted at the beginning of run PIP-22 (Fig. 4b, c). A plot of torque (stress) versus shear strain rate is nearly linear in log–log space, and is well fit with an exponent of $n = 3.4$. This is within error of the expected value for olivine deforming by dislocation creep ($n = 3.5 \pm 0.3$) (Chopra & Paterson 1984; Hirth & Kohlstedt 2003). There is some deviation at the highest strain rates, as evidenced by the curvature in Figure 4c, which is interpreted as a transition to exponential Peierls creep (e.g. Evans & Goetze 1979; Katayama & Karato 2008). The remainder of the experiments discussed here were conducted at conditions within the $n = 3.4$ regime.

Based on the value of the stress exponent we conclude that deformation is accomplished by dislocation creep. However, calculations of shear stresses from the torque data using equation (1) gives values higher than flow laws would predict. For example, sample PIP-21 had an apparent steady-state shear stress of *c.* 320 MPa while the flow law would predict shear stresses of <200 MPa. There are several possible explanations for the discrepancy. First, some torque was supported by deformation of the curved annulus where the dog-bone transitioned from narrow to

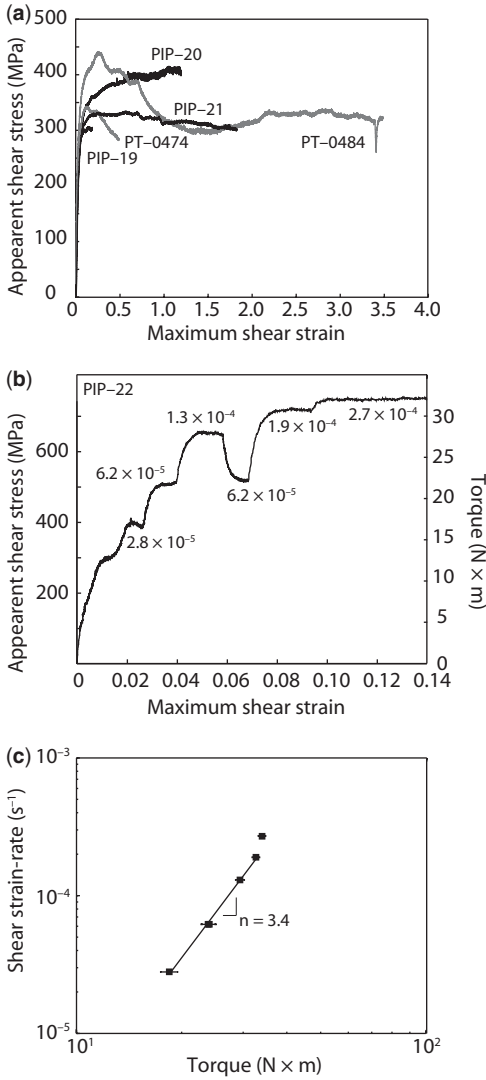


Fig. 4. Mechanical data. (a) Stress–strain curves for experiments conducted at strain rates of $2.2\text{--}4.8 \times 10^{-5} \text{ s}^{-1}$ (in black) and $1.9 \times 10^{-4} \text{ s}^{-1}$ (in grey). (b, c) Results from strain-rate stepping during experiment PIP-22. Apparent shear stress is calculated from the torque recorded by the apparatus, using equation (1).

wide; this is clearly evident from the deflection of the strain marker (Fig. 3). Because of the cubic dependence of the stress–torque relationship on sample diameter, this could easily introduce errors to the stress calculation. Similarly, the ‘fins’ in the iron jacket produced by swaging around the dog-bone shape likely introduced some error. Bystricky *et al.* (2000) also observe elevated shear stresses in comparison to flow-law predictions,

reinforcing the suggestion that this is likely a systematic problem with the geometry of the experimental design. As we discuss below, other measures of stress such as recrystallization piezometers provide numbers that are closer to flow-law predictions.

General microstructural observations

A series of experiments from shear strains of 0.2–3.9 were conducted to investigate the evolution of various microstructures (Table 1). In tangent sections through the specimens, both deformed and undeformed regions are observed (Fig. 5). Microstructures in the undeformed portion of the specimens appear unaltered in comparison to the starting materials. Deformed portions of the specimens show increasingly modified microstructures with progressive strain. As described in detail below, progressive strain modifies the pre-existing LPO. Progressive strain is also observed to alter the grain size and grain shape. Below $\gamma = 0.5$, we observe no fine-grained material that we interpret to be the product of dynamic recrystallization. Between $\gamma = 1.2$ and $\gamma = 3.5$, the amount of fine-grained material increases from less than 1% to approximately 30% by volume. This fine-grained material forms narrow bands that grow and interconnect at larger strains, and we interpret this fine-grained material to be the product of dynamic recrystallization. Relict grains often contain subgrains, but do not show any evidence of grain-boundary bulging or migration. Some fractures are seen in thin section, generally parallel to the orientation of the maximum compressive stress. These fractures are Mode I (showing no shear offset) and exhibit clear cross-cutting relationships with ductile microstructures. They are also continuous features that intersect low-strain and high-strain regions of the specimen. We therefore conclude that the fractures form during the brief interval of deformation (generally 5–30 s) that occurred after the iron jacket ruptured and before the actuator that drives deformation was manually stopped. No other fracturing that is obviously related to experimental deformation is noted.

LPO of relict grains

In all samples, sufficient relict (unrecrystallized) material remains to make LPO measurements. These data can then be compared to the undeformed portions of the samples to determine how LPO in the unrecrystallized material evolved with progressive deformation (Fig. 6). Because of the relatively large grain size in the samples, datasets are quite small (50–100 unique grains); we therefore only describe the LPO in qualitative terms. Sample

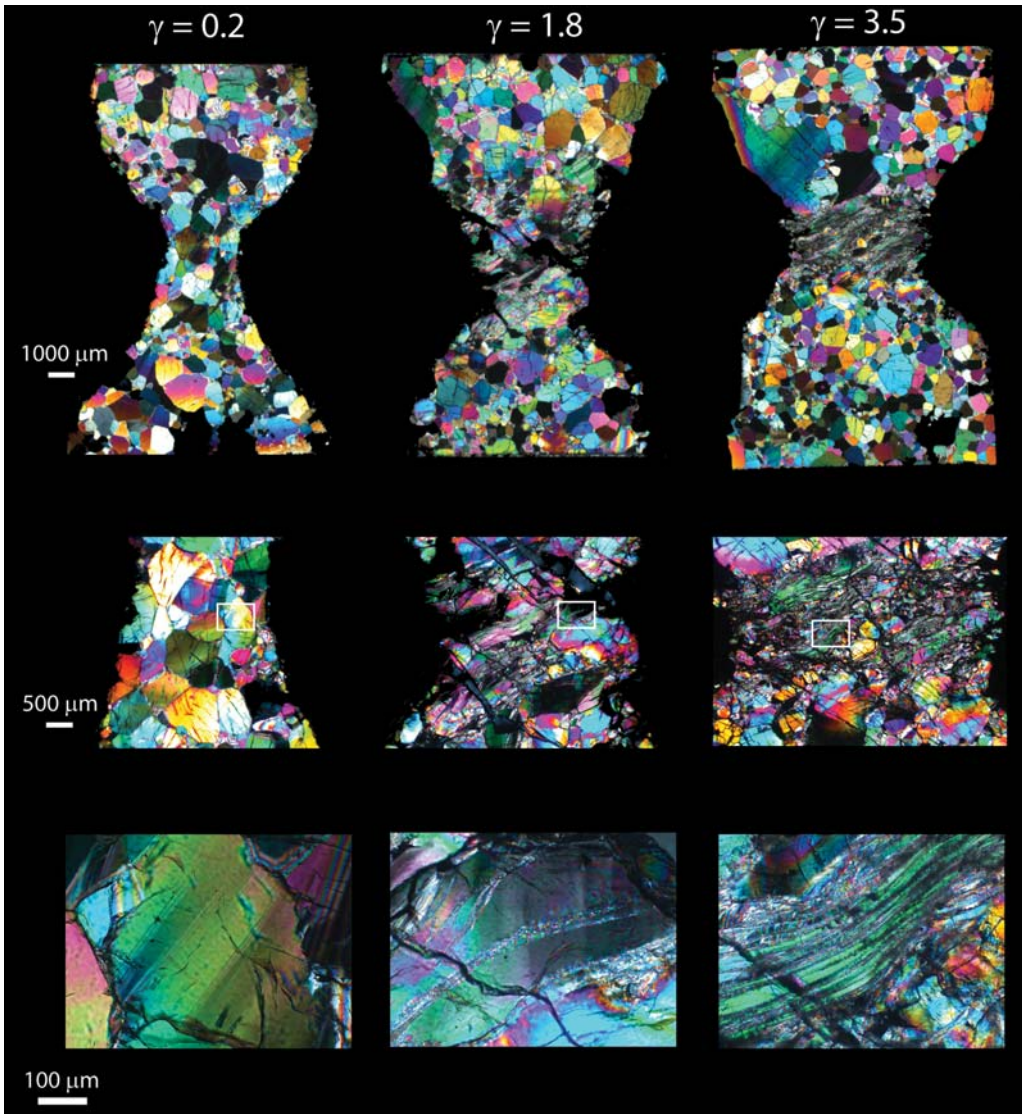


Fig. 5. Photomicrographs of samples PIP-19, PIP-21 and PT-0484 (left to right). The upper row of images shows the entire experimental charge. The middle row of images contains higher-magnification views of the deformed parts of the sample. The lower row of images shows high-magnification photomicrographs of the white inset boxes. Sense of shear is top to the right. Thin sections are nearly tangent to the edge of the deformed part of the dog-bone. Undeformed regions at the ends of the samples show no microstructural alteration, while the deformed centres of the samples show increasing microstructural alteration with strain. In the high-magnification images, recrystallized material is seen to form narrow bands which become more abundant and interconnected at higher strain.

PIP-19, which was deformed to a maximum shear strain of 0.2, exhibits little modification of the pre-existing LPO. Minor rotations of the [100] and [001] axes are detected. Sample PT-0474, deformed to $\gamma = 0.5$, also shows little alteration of the pre-existing fabric, although the maxima become somewhat less distinct. By contrast, in sample PIP-20

(which was deformed to a shear strain of 1.2) the pre-existing fabric has been completely transformed. The deformed portion of the specimen has a preferred orientation with [100] and [001] axes exhibiting partial girdles, including clusters of data at high angles to the shear plane and clusters of data in the shear plane normal to the shear direction.

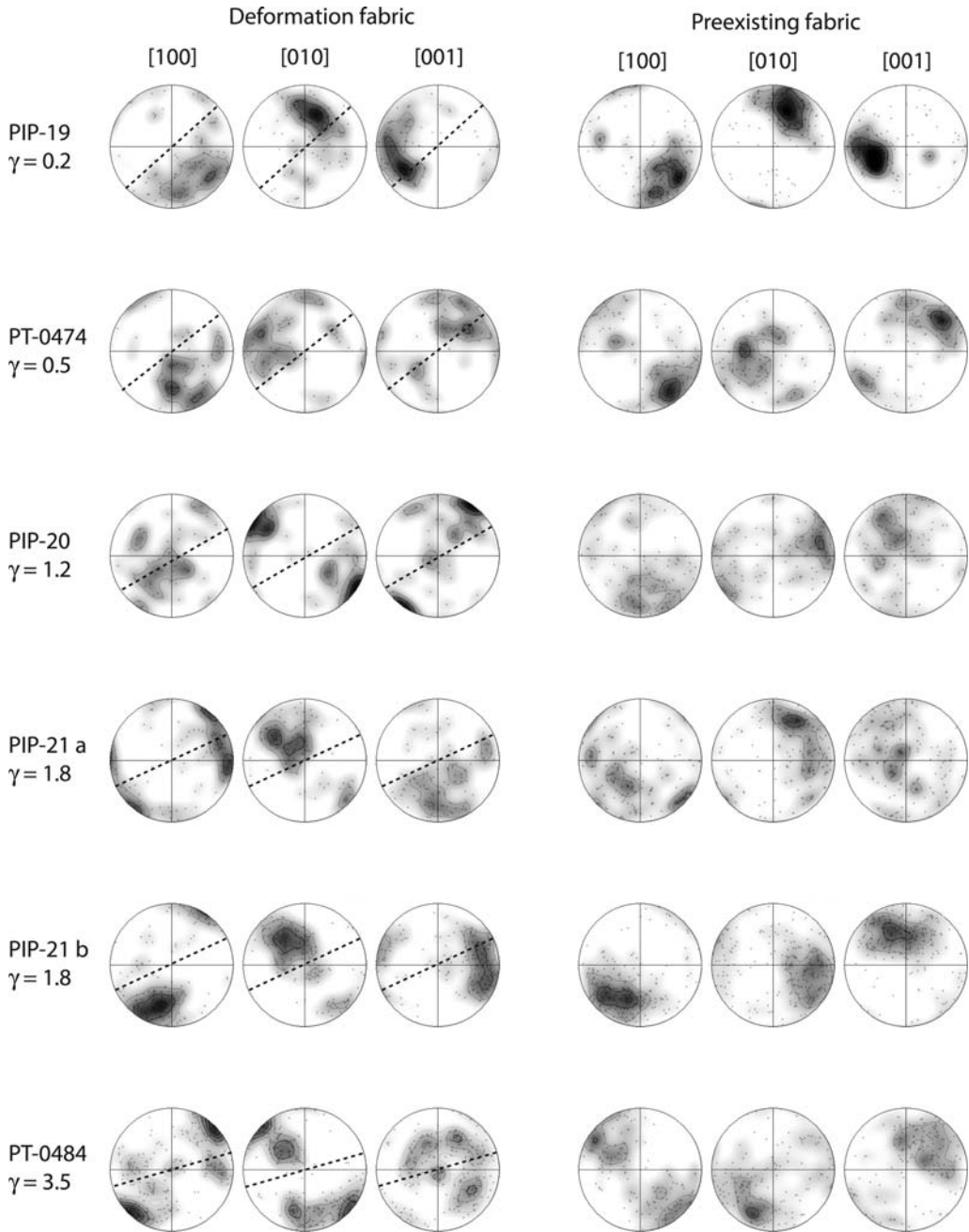


Fig. 6. Pole figures showing deformation fabrics in relict (unrecrystallized) grains and the pre-existing fabric for each sample. Pre-existing fabrics are plotted in the initial reference frame of the deformed portion of the sample. Projections are upper hemispheres, with the shear direction east–west and the pole to the shear plane north–south. Contour intervals are 1 Multiples of Uniform Distribution (MUD), with shading that saturates at 8 MUD. Small squares on each pole figure mark locations of individual data points. The sense of shear in these pole figures is dextral. Dashed lines show the orientation of the long axis of the finite strain ellipsoid. Two different sections of PIP-21 are shown; these were taken from different azimuths (separated by 135°) around the deformed sample.

The [010] axes cluster at a single point maximum, also at a high angle to the shear plane. For sample PIP-21, deformed to $\gamma = 1.8$, data were collected from two slices taken from different azimuths around the cylindrical sample (separated by 135°). Various azimuths around the cylindrical sample had different relationships between the orthorhombic starting LPO and the kinematics of deformation at that position in the sample. Analysing these data allows us to directly test the influence of the initial preferred orientation in the starting material. For these two datasets, the LPO produced by deformation is similar in the [100] and [010] directions, but deviates somewhat in the [001] direction. The [100] axes are again at a very high angle to the shear plane. Sample PT-0484, which was deformed to maximum shear strain of 3.5, displays the best developed fabric with [100] and [010] axes clustered at high angles to the shear plane and [001] axes clustered in the shear plane normal to the shear direction.

Dynamic recrystallization

Small amounts of fine-grained material (*c.* 1 vol%) first appear in sample PIP-20, which was deformed to a maximum shear strain of $\gamma = 1.2$. This fine-grained material, which we interpret to be the product of dynamic recrystallization, is organized into 10–25 μm thick bands oriented *c.* 20° to the shear plane (Fig. 7a). These bands are only a few grains wide. The preferred orientation of the material in these bands forms a great circle of [100] and [010] axes, rotated about the [001] axis. This character of deformation is also evident in inverse pole figures of misorientation axes, which highlight the strong preference for rotation about the [001] axis (Fig. 7c, e).

In sample PIP-21, deformed to $\gamma = 1.8$, fine-grained material is more abundant (*c.* 10 vol%) with bands of these grains up to *c.* 100 microns thick dissecting relict grains (Fig. 7b, d, f). Again, the crystal orientations within the bands form great circles of [100] and [010] axes, rotated about the [001] axis. Within these bands there is a complex microstructure. Some grains have very large aspect ratios, and are dissected by low-angle boundaries. The large-aspect ratio grains have serrated margins with small (*c.* 4 μm) equant grains present on the serrations. These microstructures are interpreted to be evidence of dynamic recrystallization by both subgrain rotation and nucleation and growth processes. There are varying magnitudes of internal deformation in these grains as indicated by the distortion of the crystal lattice in the EBSD data. The preferred orientation of these recrystallized grains is related to the orientation of the unrecrystallized grain through which the bands

pass (noted by white stars on the pole figures in Fig. 7). At $\gamma = 3.5$ (sample PT-0484), these bands of recrystallized grains become interconnected and form a network that dissects the relict grains into long ribbon shapes. This process results in a strongly layered microstructure within the sample, at an oblique angle to the shear plane (Fig. 5).

The recrystallized grain size provides an independent constraint on the flow stress during deformation (e.g. Twiss 1977). Although the morphology of the recrystallized grains is complicated, the mean grain size for sample PIP-21 (calculated using the mean intercept technique with a stereological correction factor of 1.75 from the image in Figure 7) is *c.* $9.2 \pm 3.0 \mu\text{m}$. Applying the recrystallization piezometry of van der Wal *et al.* (1993), this corresponds to a differential stress of $259 +88/-49 \text{ MPa}$ (Fig. 1). We note that this grain size is within error of what would be expected for olivine deforming at these conditions, based on published dislocation creep flow laws (Hirth & Kohlstedt 2003). Even the stress predicted for the smallest neoblasts (*c.* 4 μm corresponding to differential stresses of only *c.* 480 MPa; van der Wal *et al.* 1993) is significantly below the flow stresses estimated from the torque record.

Discussion

Normally it is assumed that, with increasing strain, olivine [100] crystallographic axes will tend to rotate towards the shear plane. Indeed, as we will discuss here, many experimental, numerical and geological observations have found this to be the case. However, other numerical studies (particularly those that do not explicitly include dynamic recrystallization) show that oblique LPO are retained at moderate strain. At the largest strains in this study we observe that, while the pre-existing LPO is modified, there is very little subsequent rotation of the LPO of relict unrecrystallized grains; sample PT-0484, deformed to a shear strain of 3.5, still has its [100] and [010] axes at a *c.* 45° angle to the shear plane. We now discuss our results in relation to previous studies.

Comparison of results to previous experimental and numerical studies

When fine-grained olivine aggregates are studied at typical laboratory conditions, a fraction of deformation may be accommodated by mechanisms other than dislocation creep (Fig. 1). The experiments by Zhang & Karato (1995), the first to investigate evolution of olivine LPO in general shear, were conducted on polycrystalline aggregates with a mean grain size of $<50 \mu\text{m}$ at 1473 and 1573 K.

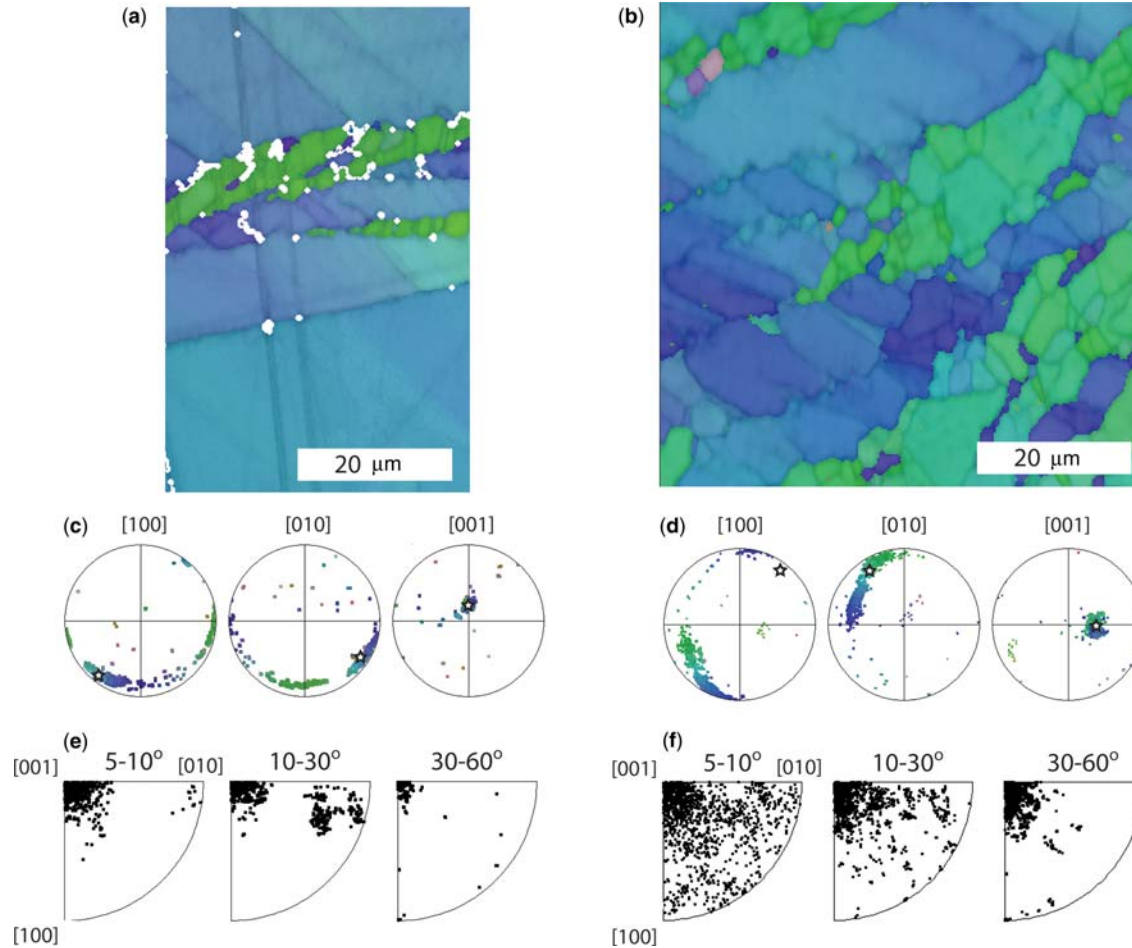


Fig. 7. EBSD data for recrystallized shear bands cross-cutting unrecrystallized grains from (a, c, e) samples PIP-20 and (b, d, f) PIP-21. (a) An EBSD map showing incipient recrystallization in sample PIP-20. The shear band at this stage is only a few grains wide. Colouration is with respect to the microscope reference frame and the band contrast of the Kikuchi patterns. (b) An EBSD map from the centre of a larger shear band in sample PIP-21. (c, d) Pole figures showing the orientations of all data within this EBSD map. The white stars show the orientation of the host parent grain. The colouration is the same as in the EBSD maps. (e, f) Inverse pole figures of misorientation axes between adjacent pixels in the EBSD maps for a range of misorientation angles. The strong clustering of data indicate that most crystallographic rotations in these regions are about the [001] axis.

At 1473 K, dynamic recrystallization was limited and occurred mainly on grain boundaries. The relict grains exhibited an LPO (specifically maxima of [100]) that nearly tracked the maximum elongation of the finite strain ellipse. At higher temperatures (1573 K), more dynamic recrystallization was observed and preferred orientations rotated into concordance with the shear plane at shear strains of *c.* 1. Even at lower temperatures, rotation of olivine LPO towards the shear plane was achieved at lower strains than we observe in our study.

Some of the samples from the Zhang & Karato (1995) study showed two clusters of crystallographic orientations, one with [100] in the shear plane and one with [100] oblique to the shear plane. These peaks were subsequently shown by Lee *et al.* (2002) to arise from different mechanisms of recrystallization. In the Lee *et al.* (2002) study, grains oblique to the shear plane were found to have low dislocation densities and interpreted to form by grain-boundary migration recrystallization. The LPO of this low dislocation density population of grains is similar to the LPO that we observed in the unrecrystallized relict grains from our study. However, in our study, the relict grains show extensive internal deformation and subgrain development. We therefore do not believe that the obliquity of [100] axes in our samples results from grain-boundary migration.

A series of experiments by Bystricky *et al.* (2000) also provide constraints on the evolution of olivine LPO. These experiments were conducted on fine-grained aggregates at 1473 K, in a torsion geometry that allowed the authors to achieve larger strains. Their results show grain-boundary-dominated recrystallization and rapid development of LPO with strong [100] maxima in the direction of shear, and girdles of [010] and [001] maxima orthogonal to the shear direction. The LPO in the fine-grained portions of our experiments do not reproduce these observations. We suggest that this discrepancy arises from differences in the distribution of the recrystallized grains. In the experiments by Bystricky *et al.* (2000), recrystallized grains formed contiguous and extensive networks along grain boundaries (even at low strain). The recrystallized material was therefore oriented and distributed in a way that facilitates accommodation of large strain in fine-grained material. In our experiments, the bands of recrystallized material form at higher angles to the shear plane and are often not interconnected; they therefore may not have accumulated much strain. This may explain why these bands of recrystallized grains exhibit LPO that is primarily related to the orientation of the host grain, rather than the macroscopic kinematics of deformation. We suggest that the differences in the distribution of recrystallized grains may be a

consequence of the difference in the initial grain size, and therefore in the density of grain-boundary nucleation sites.

Numerical models that explicitly include subgrain rotation or nucleation dominated recrystallization predict rapid rotations of the LPO towards the shear plane (e.g. Wenk & Tomé 1999; Kaminski & Ribe 2001). However, models that do not include recrystallization mechanisms show that olivine LPO may remain oblique to the shear plane at moderate strains (Wenk *et al.* 1991; Tommasi *et al.* 2000). This is partly due to the sluggish rotation of unfavourably oriented grains (Wenk *et al.* 1991). Our observations of oblique LPO in relict grains agree with numerical models in the absence of dynamic recrystallization. The absence of recrystallization in the relict grains may therefore explain the long-lived obliquity of the LPO in our samples.

Another important factor influencing the rate of LPO development may be the suppression of grain-size-sensitive processes. The large grain size in our samples means that strain incompatibilities caused by differential rotation of adjacent grains are not readily relaxed by diffusion creep, grain-boundary sliding and/or grain-boundary migration. Thus, more slip systems may be required to accommodate arbitrary strain and crystallographic rotations with respect to kinematics may be inhibited (Tommasi *et al.* 2000). We also note that in our experiments dynamic recrystallization occurs primarily in the grain interiors rather than along grain boundaries. This may have a number of consequences. First, the absence of fine-grained materials along relict grain boundaries may change the subsequent deformation of those relict grains by inhibiting diffusion creep or grain-boundary sliding; both of these diffusion-controlled processes may act to relax incompatibilities along relict grain boundaries. Also, the formation of shear bands through grains rather than along grain boundaries changes the degree to which interconnectivity of microstructures occurs. Interconnectivity of weak material is essential for macroscopic weakening of a two-part composite material (e.g. Handy 1994).

Comparison of results with geological observations

In general, geological observations of the relationships among LPO, foliation and shear plane are limited, due to the difficulty of measuring finite strain and identifying the shear plane in natural settings. Many measurements of olivine LPO from naturally deformed samples show a moderate obliquity between the [100] maximum and the foliation plane (Nicolas *et al.* 1971; Mercier 1985; Ben Ismail

& Mainprice 1998). Because finite strain (as well as the orientation of the shear plane) is often unknown, it is not however clear how much natural variation there is in the relationship between olivine LPO and the kinematics of deformation. The kinematically best-constrained examples of natural shear zones show that, with sufficient strain, olivine [100] crystallographic axes tend to rotate into the shear plane (Warren *et al.* 2008; Skemer *et al.* 2010). However, the amount of strain required is somewhat larger than inferred from laboratory experiments, which was interpreted to be a consequence of the pre-existing LPO (Warren *et al.* 2008). Pre-existing LPO is observed, both in some natural shear zones and in our experiments, to be overprinted at relatively modest strain ($\gamma \sim 1$). However, other studies have suggested that under certain conditions still larger strains may be required to obliterate pre-existing LPO (Webber *et al.* 2008, 2010), or that deformation and LPO development may be otherwise modified (Toy *et al.* 2008). The relationship between the olivine LPO and the foliation and shear planes also depends on the specific type of LPO. For example, field and experimental observations have demonstrated that the sense of obliquity between the LPO and the shear plane is different for olivine A-type and E-type LPO (Katayama *et al.* 2004; Skemer *et al.* 2010).

Our study suggests that rates of LPO development may vary more significantly than previously supposed. This is not too surprising: LPO is a very complicated phenomenon, the formation of which involves several distinct and sometimes competing physical mechanisms. LPO development is strongly influenced by the relative strengths of various slip systems (Wenk *et al.* 1991; Tommasi *et al.* 2000; Kaminski 2002; Karato *et al.* 2008). Changes in the predominance of these slip systems are known to induce changes in preferred orientation (Jung & Karato 2001). Details of the recrystallization mechanism (Urai *et al.* 1986; Wenk & Tomé 1999; Lee *et al.* 2002) or modification of LPO due to the presence of secondary phases (Warren & Hirth 2006; Sundberg & Cooper 2008; Skemer *et al.* 2010) may also alter LPO development. Indeed, in specific natural settings, LPO development is seen to vary on outcrop scales (Skemer *et al.* 2010). Further study is required to understand whether the observations in this study are solely a consequence of the starting material, the conditions of deformation or both.

Many recent geological and experimental studies have demonstrated that deformation microstructures continue to evolve at very large strains (Bystricky *et al.* 2000; Pieri *et al.* 2001; Heidelbach *et al.* 2003; Rybacki *et al.* 2003; Barnhoorn *et al.* 2005; Bystricky *et al.* 2006; Heilbronner & Tullis 2006; Warren & Hirth 2006; Skemer & Karato 2008; Warren *et al.* 2008; Skemer *et al.* 2010;

Webber *et al.* 2010). Indeed, because of the strong feedbacks between microstructure and rheology, these studies suggest that at some conditions steady-state rheology may not be achieved in materials deformed to modest strains (Mackwell & Paterson 2002). Steady-state microstructure and rheology is even more difficult to achieve in situations where deformation conditions also continue to evolve. For example, materials advected through corner-flow regimes at mid-ocean ridges and subduction zones experience changes in deformation kinematics as well as changes in temperature, pressure and chemical conditions. Evolving kinematics coupled with sluggish microstructural evolution will greatly complicate the interpretation of geophysical data (Kaminski & Ribe 2002; Castelnau *et al.* 2009). Our experiments demonstrate that, under certain conditions, we cannot always assume simple parallel relationships between LPO, seismic anisotropy and deformation kinematics.

Conclusions

We have conducted large-strain deformation experiments in torsion on a natural dunite. This starting material has a larger initial grain size and stronger initial LPO than the synthetic aggregates investigated in previous studies. These experiments are therefore conducted at conditions where secondary deformation mechanisms such as grain-boundary sliding and diffusion creep are largely suppressed. We observe that the character and rate of microstructural evolution is different than in previous studies. Specifically, we observe that considerable strain (at least $\gamma = 1$) is required to modify the pre-existing LPO. We also observe little rotation of the LPO of relict (unrecrystallized) material towards the shear plane. The LPO we observe in relict grains is similar to LPO formed numerically in the absence of dynamic recrystallization (e.g. Wenk *et al.* 1991). Additionally, we note that dynamic recrystallization occurs mainly in the grain interiors rather than along grain boundaries. We note that the rate of microstructural evolution cannot be decoupled from the initial microstructure of a sample. We conclude that both the starting microstructure of a material and the conditions of deformation play a key role in determining how subsequent microstructural evolution occurs. The interpretation of seismic anisotropy, particularly in complicated kinematic environments, must be carefully evaluated in this context.

The authors thank D. Kohlstedt for use of Paterson torsion apparatus at the University of Minnesota and T. Tullis for providing the starting material for these experiments. D. Prior, V. Toy and an anonymous reviewer are thanked for their constructive comments. This work was supported in part by NSF EAR-0911289 and EAR-0609869.

References

- BARNHOORN, A. M., BYSTRICKY, M., KUNZE, K., BURLINI, L. & BURG, J. P. 2005. Strain localization in bi-mineralic rocks: experimental deformation of synthetic calcite-anhydrite aggregates. *Earth and Planetary Science Letters*, **240**, 748–763.
- BEN ISMAIL, W. & MAINPRICE, D. 1998. An olivine fabric database; an overview of upper mantle fabrics and seismic anisotropy. *Tectonophysics*, **296**, 145–157.
- BLACKMAN, D. K. & KENDALL, J. M. 2002. Seismic anisotropy in the upper mantle 2. Predictions for current plate boundary flow models. *Geochemistry Geophysics Geosystems*, **3**, 8602.
- BYSTRICKY, M., KUNZE, K., BURLINI, L. & BURG, J. P. 2000. High shear strain of olivine aggregates; rheological and seismic consequences. *Science*, **290**, 1564–1567.
- BYSTRICKY, M., HEIDELBACH, F. & MACKWELL, S. 2006. Large-strain deformation and strain partitioning in polyphase rocks: dislocation creep of olivine-magnesiowüstite aggregates. *Tectonophysics*, **427**, 115–132.
- CARTER, N. L. & AVE LALLEMANT, H. G. 1970. High temperature flow of dunite and peridotite. *Geological Society of America Bulletin*, **81**, 2181–2202.
- CASTELNAU, O., BLACKMAN, D. K. & BECKER, T. W. 2009. Numerical simulations of texture development and associated rheological anisotropy in regions of complex mantle flow. *Geophysical Research Letters*, **36**, L12304.
- CHOPRA, P. N. & PATERSON, M. S. 1984. The role of water in the deformation of dunite. *Journal of Geophysical Research*, **89**, 7861–7876.
- EVANS, B. & GOETZE, C. 1979. Temperature-variation of hardness of olivine and its implication for polycrystalline yield stress. *Journal of Geophysical Research*, **84**, 5505–5524.
- HANDY, M. R. 1994. Flow laws for rocks containing two non-linear viscous phases; a phenomenological approach. *Journal of Structural Geology*, **16**, 287–301.
- HEIDELBACH, F., STRETTON, I., LANGENHORST, F. & MACKWELL, S. 2003. Fabric evolution during high shear strain deformation of magnesiowüstite (MgO.8FeO.2O). *Journal of Geophysical Research*, **108**, 2154.
- HEILBRONNER, R. & TULLIS, J. 2006. Evolution of c axis pole figures and grain size during dynamic recrystallization: results from experimentally sheared quartzite. *Journal of Geophysical Research*, **111**, B10202.
- HIRTH, G. & KOHLSTEDT, D. L. 2003. Rheology of the upper mantle and the mantle wedge: a view from the experimentalists, inside the subduction factory. *American Geophysical Union*, **138**, 83–105.
- JUNG, H. & KARATO, S. I. 2001. Water-induced fabric transitions in olivine. *Science*, **293**, 1460–1462.
- KAMINSKI, E. 2002. The influence of water on the development of lattice preferred orientation in olivine aggregates. *Geophysical Research Letters*, **29**, 1576.
- KAMINSKI, E. & RIBE, N. M. 2001. A kinematic model for recrystallization and texture development in olivine polycrystals. *Earth and Planetary Science Letters*, **189**, 253–267.
- KAMINSKI, E. & RIBE, N. M. 2002. Timescales for the evolution of seismic anisotropy in mantle flow. *Geochemistry, Geophysics, Geosystems*, **3**, 1051.
- KARATO, S. & WU, P. 1993. Rheology of the upper mantle: a synthesis. *Science*, **260**, 771–777.
- KARATO, S.-I., JUNG, H., KATAYAMA, I. & SKEMER, P. 2008. Geodynamic significance of seismic anisotropy of the upper mantle: new insights from laboratory studies. *Annual Review of Earth and Planetary Sciences*, **36**, 59–95.
- KATAYAMA, I. & KARATO, S. I. 2008. Low-temperature, high-stress deformation of olivine under water-saturated conditions. *Physics of the Earth and Planetary Interiors*, **168**, 125–133.
- KATAYAMA, I., JUNG, H. & KARATO, S. I. 2004. New type of olivine fabric from deformation experiments at modest water content and low stress. *Geology (Boulder)*, **32**, 1045–1048.
- LEE, K. H., JIANG, Z. & KARATO, S. I. 2002. A scanning electron microscope study of the effects of dynamic recrystallization on lattice preferred orientation in olivine. *Tectonophysics*, **351**, 331–341.
- MACKWELL, S. J. & PATERSON, M. S. 2002. New developments in deformation studies: high-strain deformation. In: KARATO, S.-I. & WENK, H.-R. (eds) *Plastic Deformation of Minerals and Rocks*. Mineralogical Society of America, Washington, D.C., 1–19.
- MERCIER, J. (ed.) 1985. Olivine and Pyroxenes. In: WENK, H.-R. (ed.) *Preferred Orientation in Deformed Metals and Rocks: An Introduction to Modern Texture Analysis*. Academic Press, Orlando, 407–430.
- NICOLAS, A. & CHRISTENSEN, N. I. 1987. Formation of anisotropy in upper mantle peridotites; a review. In: FUCHS, K. & FROIDEVAUX, C. (eds) *Composition, Structure and Dynamics of the Lithosphere-Asthenosphere System*. American Geophysical Union, Washington DC, United States, Geodynamics Series, 111–123.
- NICOLAS, A., BOUCHEZ, J. L., BOUDIER, F. & MERCIER, J. C. 1971. Textures, structures and fabrics due to solid state flow in some European lherzolites. *Tectonophysics*, **12**, 55–86.
- NICOLAS, A., BOUDIER, F. & BOULLIER, A. M. 1973. Mechanisms of flow in naturally and experimentally deformed peridotites. *American Journal of Science*, **273**, 853–876.
- PATERSON, M. S. & OLGAARD, D. L. 2000. Rock deformation tests to large shear strains in torsion. *Journal of Structural Geology*, **22**, 1341–1358.
- PIERI, M., BURLINI, L., KUNZE, K., STRETTON, I. & OLGAARD, D. L. 2001. Rheological and microstructural evolution of Carrara marble with high shear strain: results from high temperature torsion experiments. *Journal of Structural Geology*, **23**, 1393–1413.
- RYBACKI, E., PATERSON, M. S., WIRTH, R. & DRESEN, G. 2003. Rheology of calcite-quartz aggregates deformed to large strain in torsion. *Journal of Geophysical Research*, **108**, 2089.
- SKEMER, P. & KARATO, S. 2008. Sheared lherzolite xenoliths revisited. *Journal of Geophysical Research*, **113**, B07205.

- SKEMER, P., WARREN, J. M., KELEMEN, P. B. & HIRTH, G. 2010. Microstructural and rheological evolution of a mantle shear zone. *Journal of Petrology*, **51**, 43–53.
- SUNDBERG, M. & COOPER, R. F. 2008. Crystallographic preferred orientation produced by diffusional creep of harzburgite: effects of chemical interactions among phases during plastic flow. *Journal of Geophysical Research*, **113**, B12208.
- TOMMASI, A., MAINPRICE, D., CANOVA, G. & CHASTEL, Y. 2000. Viscoplastic self-consistent and equilibrium-based modeling of olivine lattice preferred orientations; implications for the upper mantle seismic anisotropy. *Journal of Geophysical Research, B, Solid Earth and Planets*, **105**, 7893–7908.
- TOY, V. G., PRIOR, D. J. & NORRIS, R. J. 2008. Quartz fabrics in the Alpine Fault mylonites: influence of pre-existing preferred orientations on fabric development during progressive uplift. *Journal of Structural Geology*, **30**, 602–621.
- TWISS, R. J. 1977. Theory and applicability of a recrystallized grain size paleopiezometer. *Pure and Applied Geophysics*, **115**, 227–244.
- URAL, J. L., MEANS, W. D. & LISTER, G. S. 1986. Dynamic recrystallization of minerals. In: HOBBS, B. E. & HEARD, H. C. (eds) *Mineral and Rock Deformation; Laboratory Studies; the Paterson Volume*. American Geophysical Union, Washington DC, United States, Geophysical Monograph, 161–199.
- VAN DER WAL, D., CHOPRA, P., DRURY, M. & FITZ, G. J. 1993. Relationships between dynamically recrystallized grain size and deformation conditions in experimentally deformed olivine rocks. *Geophysical Research Letters*, **20**, 1479–1482.
- WARREN, J. M. & HIRTH, G. 2006. Grain size sensitive deformation mechanisms in naturally deformed peridotites. *Earth and Planetary Science Letters*, **248**, 438–450.
- WARREN, J. M., HIRTH, G. & KELEMEN, P. 2008. Evolution of lattice-preferred orientation during simple shear in the mantle. *Earth and Planetary Science Letters*, **272**, 501–512.
- WEBBER, C., LITTLE, T., NEWMAN, J. & TIKOFF, B. 2008. Fabric superposition in upper mantle peridotite, Red Hills, New Zealand. *Journal of Structural Geology*, **30**, 1412–1428.
- WEBBER, C., NEWMAN, J., HOLYOKE, C. W. III, LITTLE, T. & TIKOFF, B. 2010. Fabric development in cm-scale shear zones in ultramafic rocks, Red Hills, New Zealand. *Tectonophysics*, **489**, 55–75.
- WENK, H.-R. & TOMÉ, C. N. 1999. Modeling dynamic recrystallization of olivine aggregates deformed in simple shear. *Journal of Geophysical Research*, **104**, 25 513–25 527.
- WENK, H.-R., BENNETT, K., CANOVA, G. R. & MOLINARI, A. 1991. Modeling plastic-deformation of peridotite with the self-consistent theory. *Journal of Geophysical Research-Solid Earth and Planets*, **96**, 8337–8349.
- ZHANG, S. & KARATO, S. I. 1995. Lattice preferred orientation of olivine aggregates deformed in simple shear. *Nature (London)*, **375**, 774–777.
- ZHANG, S., KARATO, S. I., FITZ, G. J., FAUL, U. H. & ZHOU, Y. 2000. Simple shear deformation of olivine aggregates. *Tectonophysics*, **316**, 133–152.